Rigorous modal analysis of plasmonic nanoresonators

Wei Yan,* Rémi Faggiani, and Philippe Lalanne†
Laboratoire Photonique, Numérique et Nanosciences (LP2N), IOGS − Univ. Bordeaux − CNRS, 33400 Talence cedex, France

(Received 17 July 2017; revised manuscript received 4 April 2018; published 15 May 2018)

The specificity of modal-expansion formalisms is their capabilities to model the physical properties in the natural resonance-state basis of the system in question, leading to a transparent interpretation of the numerical results. In electromagnetism, modal-expansion formalisms are routinely used for optical waveguides. In contrast, they are much less mature for analyzing open non-Hermitian systems, such as micro- and nanoresonators. Here, by accounting for material dispersion with auxiliary fields, we considerably extend the capabilities of these formalisms, in terms of computational effectiveness, number of states handled, and range of validity. We implement an efficient finite-element solver to compute the resonance states, and derive closed-form expressions of the modal excitation coefficients for reconstructing the scattered fields. Together, these two achievements allow us to perform rigorous modal analysis of complicated plasmonic resonators, being not limited to a few resonance states, with straightforward physical interpretations and remarkable computation speeds. We particularly show that, when the number of states retained in the expansion increases, convergence toward accurate predictions is achieved, offering a solid theoretical foundation for analyzing important issues, e.g., Fano interference, quenching, and coupling with the continuum, which are critical in nanophotonic research.

DOI: 10.1103/PhysRevB.97.205422

I. INTRODUCTION

The control of light at the nanoscale is ultimately limited by our capability to engineer electromagnetic near-fields with several nanoresonances, enable energy transfers between them, and model how every individual state precisely interferes to create new resonant states that overlap in space and energy. Optical nanoresonators, be they plasmonic, photonic, or both, offer a unique route to enhance and localize the electromagnetic energy at wavelength or subwavelength scales. They now play a leading role in many areas in nanophotonics, from quantum information processing to ultrasensitive biosensing, nonlinear optics, and various optical metasurfaces.

Classically, the resonant interaction of light with optical resonances is modeled via continuum scattering theory with Maxwell solvers operating in the time- or real-frequency domains. As they do not explicitly compute the resonance states, the numerical predictions are not always easy to interpret—-the black-box sensation often experienced by users. They additionally require many computations that must be repeated for every individual frequency in the frequency domain, or in the time domain for every instance of the driving field, e.g., the pulse duration, polarization, and incidence angle [1,2]. In sharp contrast, the present formalism operates at complex frequencies $\tilde{\omega}$ set by the natural states of the resonator, also called quasinormal modes (QNMs). It offers two decisive advantages. It brings the physics of the resonant states at the heart of the analysis, thus removing the black-box sensation. It also allows one to model properties that span over a frequency range $\sim\mathrm{Im}(\tilde{\omega})$ around a central frequency $\mathrm{Re}(\tilde{\omega})$ with a high degree of analyticity, which often offer unprecedented modeling capabilities and computational performance. The formalism belongs to the general category of modal formalisms, and as such, is expected to bring a valuable input to resonance optics, comparable to that previously brought by the guided-mode theory to integrated optics design [3,4].

The spectral representation of waves in resonant systems as a superposition of QNMs has a venerable story [5–9]. In electromagnetism, pioneer works initially focused on simple geometries, e.g., 1D and 3D-spherical resonators in uniform backgrounds, for which the completeness of QNM expansions was established [10,11]. Important follow-up results were concerned with extensions of these founding works toward arbitrary resonant geometries. They include a mathematically sound normalization and definition of the mode volume [12–15], the derivation of orthogonality relation for QNMs of nondispersive resonators [10,12,16], the elaboration of perturbation methods for calculating the QNMs of a resonator from the knowledge of the QNMs of another unperturbed resonator [16–19], and attempts to implement numerically stable methods to compute and normalize QNMs [20–25]. For a recent review, see Ref. [15].

Many ingredients toward a complete modal theory of nanoresonators are now available, but they are scarcely presented and often restricted to peculiar geometries. Hereafter, we extend these works to propose a comprehensive theoretical framework for the most general case of 3D resonators with arbitrary shapes and materials, possibly in nonuniform backgrounds. The generality and effectiveness of the framework are validated by implementing an effective QNM-expansion software. Of particular importance in the present context is the successful generalization of the auxiliary-field method, originally proposed for simulating dispersive media with finite-difference time-domain simulations [26] and computing

*Correspondence author: wyanzju@gmail.com
†Corresponding author: philippe.lalanne@institutoptique.fr

the band diagram of dispersive crystals [27], to compute the QNMs of open resonators with finite-element methods (FEMs). This allows us to successfully implement a QNM solver that efficiently computes the eigenstates of plasmonic resonators. The achieved precision is much better than those offered by finite-difference approaches [21,27], especially for the usual cases of metallic nanoresonators with curved shapes. On the theoretical side, another important consequence of the auxiliary-field method is a net physical interpretation of temporal dispersion, which led us to derive orthogonality relations in the augmented formulation for resonances made of dispersive media. Such a derivation that was not possible in earlier works with unspecified dispersion relation [12,15] leads to the important proposition of closed-form expressions for the eigenstate excitation coefficients.

We believe that the joint effort in numerics and theory greatly expands the capabilities of analyzing electromagnetic resonance in nanophotonics, offering increased physical insight and improved computational speed. This brings us closer to a comprehensive modal theory of optical resonances, the analog of the optical waveguide theory for nanoresonators.

II. AUGMENTED-FIELD QNM FORMULATION

The QNMs of localized resonators, made of dispersive or non-dispersive media or both, are defined as the time-harmonic solutions to the source-free Maxwell's equations

$$\begin{bmatrix} 0 & -i\mu_0^{-1}\nabla\times \\ i\varepsilon(\tilde{\omega}_m)^{-1}\nabla\times & 0 \end{bmatrix}\begin{bmatrix} \tilde{\mathbf{H}}_m \\ \tilde{\mathbf{E}}_m \end{bmatrix} = \tilde{\omega}_m \begin{bmatrix} \tilde{\mathbf{H}}_m \\ \tilde{\mathbf{E}}_m \end{bmatrix}, \quad (1)$$

with $\varepsilon(\tilde{\omega}_m)$ the permittivity and μ_0 the vacuum permeability, an $\exp(-i\tilde{\omega}_m t)$ dependence being assumed for time-harmonic fields. The QNMs defined by their electric- and magnetic-field vectors, $\tilde{\mathbf{E}}_m$ and $\tilde{\mathbf{H}}_m$, satisfy the outgoing-wave conditions, have complex frequency $\tilde{\omega}_m$ with quality factor $Q_m = -\frac{1}{2}\mathrm{Re}(\tilde{\omega}_m)/\mathrm{Im}(\tilde{\omega}_m)$, and grow exponentially at a large distance from the structure [15].

For dispersive materials, a difficulty arises as the eigenproblem of Eq. (1) no longer defines a standard linear eigenproblem. The nonlinearity, which essentially arises from hidden variables that are eliminated in the constitutive relations, has a prescribed nature. At optical frequencies, most material properties can be modeled with a standard N-pole Lorentz-Drude relationship [27,28], $\varepsilon(\omega) = \varepsilon_\infty - \varepsilon_\infty \sum_i \omega_{p,i}^2(\omega^2 - \omega_{0,i}^2 + i\omega\gamma_i)^{-1}$, with notations for the plasma frequencies $\omega_{p,i}$, the damping coefficients γ_i, and the resonant frequencies $\omega_{0,i}$. In metals, for instance, the intraband transition gives rise to free-electron behavior characterized by a Drude pole ($\omega_{0,i} = 0$), whereas interband transitions are faithfully represented by Lorentz poles ($\omega_{0,i} \neq 0$) [28]. As already noted in Refs. [21,27], the nonlinear eigenproblem for Lorentz-Drude materials can be cast into a linear one by reintroducing hidden auxiliary fields, such as the polarization $\mathbf{P}_i = -\varepsilon_\infty\omega_{p,i}^2(\omega^2 - \omega_{0,i}^2 + i\omega\gamma_i)^{-1}\mathbf{E}$ and the current $\mathbf{J}_i = -i\omega\mathbf{P}_i$. Considering a single Lorentz-pole permittivity to simplify the notations and denoting by $\tilde{\psi}_m = [\tilde{\mathbf{H}}_m, \tilde{\mathbf{E}}_m, \tilde{\mathbf{P}}_m, \tilde{\mathbf{J}}_m]^{\mathbf{T}}$ the augmented eigenvector, Eq. (1) is reformulated in a linear form

$$\hat{\mathbf{H}}\tilde{\psi}_m = \begin{bmatrix} 0 & -i\mu_0^{-1}\nabla\times & 0 & 0 \\ i\,\varepsilon_\infty^{-1}\nabla\times & 0 & 0 & -i\varepsilon_\infty^{-1} \\ 0 & 0 & 0 & i \\ 0 & i\omega_p^2\varepsilon_\infty & -i\omega_0^2 & -i\gamma \end{bmatrix}\tilde{\psi}_m = \tilde{\omega}_m\tilde{\psi}_m, \quad (2)$$

in the Lorentz-material subspace and takes the usual form without auxiliary fields elsewhere.

A. Discretized versus continuous operators: QNM and perfectly matched layer (PML) modes

We should bear in mind that the following numerical and theoretical results are all obtained for a slightly different version of the original physical problem, in which the original open space is replaced by a finite space bounded with PMLs implementing the outgoing-wave conditions. Thus the continuous operator [Eq. (2)], originally defined on an unbounded space, after the PML mapping and numerical discretization, is replaced by an analytically continued, discretized operator (a finite-dimensional matrix) defined on a finite mapped space, with new permittivity and permeability distributions that accommodate the PMLs. With classical frequency-domain Maxwell solvers, the matrix $\hat{\mathbf{H}} - \omega\hat{\mathbf{I}}$ ($\hat{\mathbf{I}}$ being the identity matrix) is inverted for each frequency ω in order to compute the electromagnetic response to an external source. Since the discretization and the PMLs are effective only within a finite frequency interval (or domain $\mathcal{F}$ of the complex-ω plane), the electromagnetic solutions of the analytically continued operator are accurate only for frequencies within $\mathcal{F}$.

Here, instead of inverting $\hat{\mathbf{H}}$ for every frequency, we consider the discrete spectrum of $\hat{\mathbf{H}}$, and reconstruct the electromagnetic solution *analytically* from the spectral decomposition. Since $\hat{\mathbf{H}}$ is linear, using the matrix inversion scheme or the spectral decomposition approach leads to the same results (up to numerical uncertainty), i.e., the spectral decomposition approach provides exactly the same solutions as the inversion approach, if the whole set of eigenstates is considered. In particular, we get the same faithful solutions within $\mathcal{F}$, and even more importantly, the QNMs of the original continuous operator with $\tilde{\omega}_m \in \mathcal{F}$ are accurately recovered in the spectrum of $\hat{\mathbf{H}}$ and the physics—-the natural resonances—-is preserved. Advantageously, the mapped eigenstates do not grow exponentially, become square-integrable, and can be normalized [12]. In addition, complicated theoretical issues on the completeness of QNM expansions for open spaces are avoided. Indeed, the eigenstates of $\hat{\mathbf{H}}$ form a complete set over the whole mapped space, in contrast with the QNMs of the open system that form, at best, a complete set only "inside the resonator" [10]. This has important consequences for instance for plasmonic dimers like bowtie antennas, since by including the PML modes the expansion becomes complete even outside the metal, for instance in the dielectric gap where interesting phenomena occur due to the strong field enhancement.

The eigenstates of the mapped operator are composed of two sets of modes, a subset of the QNMs of the original continuous operator and a set of numerical modes, called hereafter PML modes [15,29], which depend on the PML

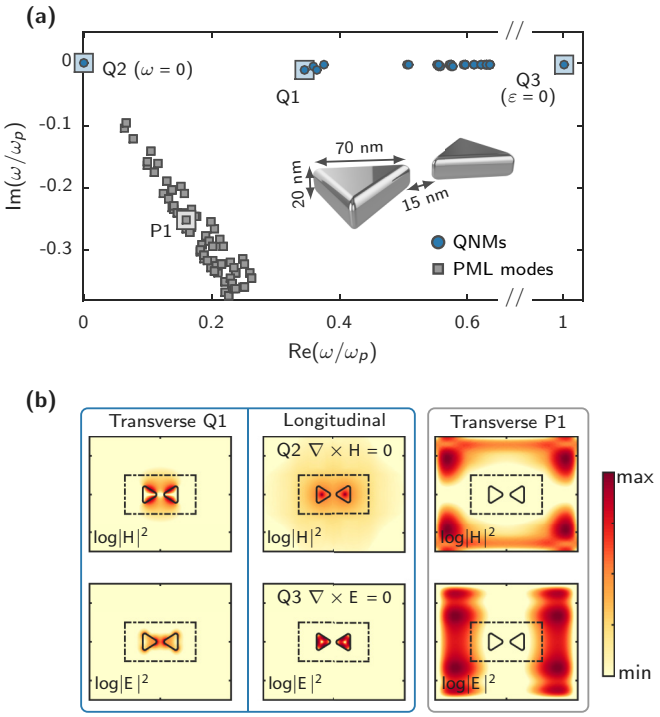

FIG. 1. QNMs and PML modes of a silver bowtie nanoantenna. The bowtie parameters are given in the inset in (a) and the rounding radius of the corner is 8 nm. (a) Eigenstate energies and decay rates computed with the auxiliary-field solver. The measured silver permittivity [35] is approximated by a realistic Drude model with $\lambda_p = 2\pi c/\omega_p = 138\,\text{nm}$ and $\gamma = 0.0023\omega_p$. Note that the eigenstates always coexist pairwise, $\tilde{\psi}_m$ at $\tilde{\omega}_m$ and $\tilde{\psi}_m^*$ at $-\tilde{\omega}_m^*$ as implied by the Hermitian symmetry $\varepsilon(\tilde{\omega}_m) = \varepsilon^*(-\tilde{\omega}_m^*)$, and that we have represented only the eigenstate subset with positive real energies, which are revealed by our nondispersive PMLs. (b) Intensity distributions of the normalized QNMs $Q1$, $Q2$, $Q3$, and the PML mode $P1$. We highlight a typical feature of the PML modes that their field intensities are dominantly located in the PML, the region outside the dashed-dotted box.

parameters and form a complete basis with the QNM subset. The PML modes can be further classified into two subclasses. The first class is fed with distorted remnants of the original QNMs with $\tilde{\omega}_m \notin \mathcal{F}$, which cannot be recovered with the discretized operator. The second class originates from the continuum of background modes [29,30]. For thick PMLs, they are Fabry-Perot modes of closed resonators mainly formed by the PMLs, and are composed of ingoing and outgoing waves in the PMLs, unlike QNMs. For uniform backgrounds, this second class of eigenstates is easily detected as it forms a tilted straight line in the complex plane, as in Fig. 1(a), resulting from a rotation by the complex stretching of the PMLs of the original continuum of plane waves that lies on the real-frequency axis [29,30]. For nonuniform backgrounds, the locations of the PML mode and QNMs in the complex plane are entangled, and disentangling may be challenging as illustrated with the last numerical example of the article. Supplemental Material, Sec. 3.4 [31] provides more details on how one may distinguish QNMs and PML modes in this case. However, the distinction is not always required, as in general, both QNMs and PML modes have to be considered in the expansion for numerical accuracy.

B. QNM eigensolver implementation

Based on Eq. (2), we have developed a QNM solver using the COMSOL MULTIPHYSICS environment [32]. For that purpose, Eq. (2) is first transformed into a standard quadratic eigenvalue problem

$$\hat{\mathbf{K}}\begin{bmatrix}\tilde{\mathbf{E}}_m\\ \tilde{\mathbf{P}}_m\end{bmatrix} + \tilde{\omega}_m\hat{\mathbf{C}}\begin{bmatrix}\tilde{\mathbf{E}}_m\\ \tilde{\mathbf{P}}_m\end{bmatrix} + \tilde{\omega}_m^2\hat{\mathbf{M}}\begin{bmatrix}\tilde{\mathbf{E}}_m\\ \tilde{\mathbf{P}}_m\end{bmatrix} = 0, \tag{3}$$

for which stable and efficient algorithms exist [33]. In Eq. (3), $\hat{\mathbf{K}} = \left[\begin{smallmatrix}\nabla\times\mu_0^{-1}\nabla\times & 0\\ \varepsilon_\infty\omega_p^2 & -\omega_0^2\end{smallmatrix}\right]$ is the stiffness matrix, $\hat{\mathbf{C}} = \left[\begin{smallmatrix}0 & 0\\ 0 & i\gamma\end{smallmatrix}\right]$ is the damping matrix, and $\hat{\mathbf{M}} = \left[\begin{smallmatrix}-\varepsilon_\infty & -1\\ 0 & 1\end{smallmatrix}\right]$ is the mass matrix. Then, the coupled system of partial differential equations is converted into its equivalent weak formulations that are entered directly in the COMSOL environment using the user COMSOL-interface framework for partial differential equations. Finally, the discretized equations are solved with the built-in iterative eigensolver of COMSOL.

The solver could be conveniently used to compute the QNMs and PML modes of arbitrary, 3D plasmonic resonators in complex photonic environments, e.g., resonators on substrates. It takes full advantage of the power of finite-element meshes to accurately model geometries mixing curved shapes, large-scale features, e.g., planar interfaces, and small-scale features, e.g., sharp corners, which ensures superior accuracy and performance compared to previous solvers developed with finite-difference discretization schemes [21,27]. Moreover, since the additional auxiliary fields are restrictively defined in the computational subspaces with dispersive materials only, the matrix-size increase due to the auxiliary fields remains moderate. Details of the weak-formulation and numerical tests of the solver performance can be found in Supplemental Material, Sec. 4 [31].

To illustrate the QNM-solver capabilities, we consider a silver bowtie antenna in a uniform air background with a permittivity $\varepsilon_b = 1$. Figure 1(a) shows the energies and decay rates of the eigenstates computed with the solver. QNMs and PML modes are shown with blue circles and gray squares, respectively. The QNMs can be decomposed into two subsets. "Transverse" QNMs satisfying $\nabla\cdot\varepsilon(\tilde{\omega}_m)\tilde{\mathbf{E}}_m = 0$ and $\nabla\cdot\mu_0\tilde{\mathbf{H}}_m = 0$ are obtained for $\tilde{\omega}_m \neq 0$ and are directly computed with the solver. This large subset is enriched by longitudinal QNMs, including bulk plasmons with nonzero eigenfrequencies $\tilde{\omega}_\text{B}$ such that $\varepsilon(\tilde{\omega}_\text{B}) = 0$, and static QNMs computed by solving $\nabla\times\tilde{\mathbf{E}}_m = 0$ (electric static) or $\nabla\times\tilde{\mathbf{H}}_m = 0$ (magnetic static); in this case, electric static QNMs have null electric fields inside resonators since $\varepsilon\to\infty$ as $\omega\to 0$. Figure 1(b) shows the intensity distributions of four eigenstates, marked with large squares in Fig. 1(a).

In Ref. [34], we provide the COMSOL models and the companion MATLAB programs that we have developed for this work. They can be easily reused and updated by drawing new geometries with the COMSOL graphical user interface.

III. RECONSTRUCTION: ORTHOGONALITY RELATION, MODAL EXCITATION COEFFICIENTS

Because it explicitly considers the physical origin of the dispersion in the constitutive relation, the augmented formulation offers a number of advantages compared to nonlinear eigenvalue formulations based on electric and magnetic fields only. For instance, as shown in Supplemental Material, Sec. 2.2, it enables an explicit distinction between different forms of the QNM energy at complex frequencies, including the kinetic energy of electrons, Ohmic absorption, and radiation leakage, which is not directly available otherwise. It additionally allows the derivation of important relationships, such as an orthogonality relation and a closed-form expression for the modal excitation coefficients used in the spectral representation of waves as superpositions of QNMs. The derivations do not require sophisticated mathematics, and are provided in their entirety in Supplemental Material, Sec. 3. Hereafter, we just summarize the main results used for the numerical examples presented in the next section. These results are valid for the general case of nanoresonators composed of dispersive materials placed in nonuniform backgrounds.

The orthogonality relation between the whole set of PML modes and QNMs for dispersive nanoresonators directly follows from the unconjugated Lorentz reciprocity theorem applied to the augmented formulation [31], and takes the following form:

$$\begin{aligned}&\langle\tilde{\psi}_n^*|\hat{\mathbf{D}}|\tilde{\psi}_m\rangle_{V_c}\\&=\iiint_{V_c}\left[\varepsilon_\infty\tilde{\mathbf{E}}_n\cdot\tilde{\mathbf{E}}_m-\mu_0\tilde{\mathbf{H}}_n\cdot\tilde{\mathbf{H}}_m\right.\\&\left.+\omega_0^2/\left(\varepsilon_\infty\omega_p^2\right)\tilde{\mathbf{P}}_n\cdot\tilde{\mathbf{P}}_m-1/\left(\varepsilon_\infty\omega_p^2\right)\tilde{\mathbf{J}}_n\cdot\tilde{\mathbf{J}}_m\right]d^3\mathbf{r}=\delta_{nm},\end{aligned}\tag{4}$$

with $\delta_{nm}=1$ if $n=m$ and 0 otherwise, $\hat{\mathbf{D}}=\mathrm{diag}[-\mu_0,\varepsilon_\infty,\omega_0^2/(\varepsilon_\infty\omega_p^2),-1/(\varepsilon_\infty\omega_p^2)]$. V_c denotes the volume of the entire mapped space, including the PMLs. It is additionally easy to show that the normalization condition $\langle\tilde{\psi}_m^*|\hat{\mathbf{D}}|\tilde{\psi}_m\rangle_{V_c}=1$ can be simply rewritten as $\iiint_{V_c}[\frac{\partial\tilde{\omega}_m\varepsilon(\tilde{\omega}_m)}{\partial\tilde{\omega}_m}\tilde{\mathbf{E}}_m\cdot\tilde{\mathbf{E}}_m-\mu_0\tilde{\mathbf{H}}_m\cdot\tilde{\mathbf{H}}_m]\,d^3\mathbf{r}=1$, consistently with earlier works [10,12,14,36]. Note that no energy consideration with conjugate scalar products is underpinned by Eq. (4). We emphasize that Eq. (4) differs from the orthogonality relation proposed in Ref. [27] for pseudoperiodic auxiliary fields of Bloch modes of plasmonic crystals, owing to the non-Hermitian character of the present QNM eigenvalue problem. Besides, it was not reported in all previous works on QNMs of dispersive resonators with nonlinear eigenvalue problem formulations based on electric and magnetic fields only, for which it was shown that QNMs are not orthogonal, see for instance Eqs. (5) and (6) in Ref. [12] and Fig. 8 in Ref. [15].

The second important result concerns the spectral representation of the field-scattered $\Psi_{\mathrm{sca}}(\mathbf{r},\omega)$ at real-frequency ω by any resonator (reconstruction problem)

$$\Psi_{\mathrm{sca}}(\mathbf{r},\omega)=\sum_m\alpha_m(\omega)\tilde{\psi}_m(\mathbf{r}),\tag{5}$$

for which it is possible to derive a closed-form expression for the excitation modal coefficients [31]

$$\begin{aligned}\alpha_m(\omega)=&\frac{\tilde{\omega}_m}{\tilde{\omega}_m-\omega}\langle\tilde{\mathbf{E}}_m^*|\varepsilon(\tilde{\omega}_m)-\varepsilon_b|\mathbf{E}_{\mathrm{inc}}(\omega)\rangle_{V_{\mathrm{res}}}\\&+\langle\tilde{\mathbf{E}}_m^*|\varepsilon_b-\varepsilon_\infty|\mathbf{E}_{\mathrm{inc}}(\omega)\rangle_{V_{\mathrm{res}}},\end{aligned}\tag{6}$$

valid for any near- or far-field illumination. In Eq. (6), ε_b is the relative permittivity of the medium surrounding the resonator, $\langle\tilde{\mathbf{E}}_m^*|f(\boldsymbol{r})|\mathbf{E}_{\mathrm{inc}}(\omega)\rangle_{V_{\mathrm{res}}}=\iiint_{V_{\mathrm{res}}}f(\boldsymbol{r})\tilde{\mathbf{E}}_m\cdot\mathbf{E}_{\mathrm{inc}}(\omega)d^3\boldsymbol{r}$ is the usual overlap integral involving the resonance mode and the driving field , V_{res} being the resonator domain used for the scattered-field formulation, and $f(\boldsymbol{r})$ a weighting function. Equations (5) and (6) provide a high level of analyticity for the reconstruction step.

As will be evidenced by the following numerical results, the natural resonances, QNMs of the continuous operator are largely recovered in the spectrum of the mapped operator, and thus the set of eigenvectors $\tilde{\psi}_m(\mathbf{r})$ constitutes a basis of predilection to model the resonator, explicitly highlighting Fano-like interferences between the dominant eigenvectors. In addition, assuming the absence of any accidental degeneracies at exceptional points for instance [37], the eigenvectors form a complete set over the whole mapped space and the QNM expansion provides highly accurate predictions—in Ref. [31], we show the following closure relation: $\sum_{m=1}^{\infty}\tilde{\psi}_m(\mathbf{r}')\tilde{\psi}_m^{\mathrm{T}}(\mathbf{r})\hat{\mathbf{D}}=\hat{\mathbf{I}}\delta(\mathbf{r}-\mathbf{r}')$, $\hat{\mathbf{I}}$ being an identity matrix and the superscript "T" being the transpose operator. It is important to bear in mind that Eq. (5), like the closure relation, holds for any $\mathbf{r}$ in the whole mapped space, including the PMLs, in sharp contrast with QNM expansions of open systems that are strictly exact only "inside the resonator" [10,11].

Equations (5) and (6) will be repeatedly used for the following numerical results obtained for various nanoresonator geometries and driving illuminations. All eigenvectors do not play the same role in those equations. To realize what the dominant eigenvectors could be, we again consider the spectrum of continuous operators. From rigorous mathematical proof obtained for simple 1D and 3D spherically symmetric resonators geometries, it is widely accepted that the (true) QNM set forms a complete basis, provided that the electromagnetic Green's tensor $\mathbf{G}(\omega,\mathbf{r}',\mathbf{r})$ is analytic in the complex-frequency plane excluding the QNM poles and that $\mathbf{r}$ and $\mathbf{r}'$ are inside the resonator [10,11]. This implies that for simple geometries, such as 3D resonators in uniform dielectric backgrounds, the PML modes of the mapped operator are expected to play a nondominant role in the expansion of Eq. (5). Thus, provided that the PML mapping preserves the dominant QNMs of the open space, accurate predictions are expected for the scattered field with only QNMs, only for simple geometries. This result will be illustrated by numerical results hereafter.

IV. NUMERICAL RESULTS AND VALIDATION

With a few selected examples, we test the theoretical results with what is happening on the ground and assess the modeling capabilities of the QNM-expansion formalism, either for clarifying the physics of resonant systems based on the interference of a few modes or for accurately analyzing complex situations involving many modes of different nature.

Other pertaining tests on the computational speed, the exactness, or the convergence as a function of the number of eigenstates retained in the expansion of Eq. (5) are outlined in Supplemental Material, Sec. 5 [31].

A. Spectral and temporal analysis of antenna in uniform backgrounds

The first example concerns a bowtie antenna in air. The first motivation for studying this relatively simple geometry is to illustrate the importance of QNMs, comparatively to PML modes, for resonators with uniform backgrounds, by showing that the convergence rate is dominantly driven by QNMs in this case and that PML modes convey minor additional information that is required only if a high accuracy is desired. Another motivation is to lay new foundations for modal expansions in the temporal domain, which has received only little attention in the literature to our knowledge [38]. It is yet another motivation to show that the modal approach provides a physical insight that is difficult to get with other standard Maxwell's equation solvers operating in the time or spectral domains.

Using Eqs. (5) and (6), we have computed the optical response of the bowtie antenna under illumination by a normally incident plane wave polarized along the bowtie axis. A rapid study of the convergence of the QNM expansion as a function of the truncation rank, i.e., the number M of QNMs retained in the expansion, has revealed that no more than ten QNMs have a significant impact on the extinction and absorption cross-section spectra in the visible. Note that the longitudinal QNMs are not excited since the excitation of bulk plasmons require free electric charges inside resonators and static QNMs have null electric fields inside resonators; the contribution of PML modes is weak. Figure 2(a) compares the predictions of the modal method for $M = 12$ [the QNM eigenfrequencies are illustrated in the inset of Fig. 2(b)] with full-wave frequency data obtained with the classical frequency-domain solver of COMSOL MULTIPHYSICS. The agreement is quantitative over the entire spectrum, and can be further improved to reach an absolute accuracy of 10^{-3} by including PML modes in the modal expansion; see Fig. SI.6 in Supplemental Material.

To illustrate the versatility of the QNM expansion, we further consider the bowtie response in the temporal domain. Nanoresonator dynamics are important to explore new spatial and temporal regimes by controlling light-matter interactions with nanometric and femtosecond precisions [39,40]. The spectral QNM expansion of Eq. (5) admits a simple sister form in the temporal domain

$$\Psi_{\rm sca}(\mathbf{r},t) = \sum_m \beta_m(t)\tilde{\psi}_m(\mathbf{r}), \tag{7}$$

with $\beta_m(t) = \int_{-\infty}^{+\infty} \alpha_m(\omega)\exp(-i\omega t)\mathrm{d}\omega$, where $\alpha_m(\omega)$ is weighted by the spectral power density $\mathbf{E}_{\rm inc}(\omega) = \int_{-\infty}^{+\infty} \mathbf{E}_{\rm inc}(t)\exp(i\omega t)\mathrm{d}t/2\pi$ of the driving pulse $\mathbf{E}_{\rm inc}(t)$. In our implementation, $\beta_m(t)$ is conveniently computed with a fast Fourier transform algorithm. However, to obtain more insight, it is worth performing the calculation analytically by using contour integration. Injecting the expression of $\mathbf{E}_{\rm inc}(\omega)$ into Eq. (6) to express $\alpha_m(\omega)$ in terms of $\mathbf{E}_{\rm inc}(t)$, and then using the Cauchy integral formula for the pole at $\omega = \tilde{\omega}_m$, we obtain

$$\beta_m(t) = \langle \tilde{\mathbf{E}}_m^* | i\tilde{\omega}_m(\varepsilon_m(\tilde{\omega}_m) - \varepsilon_b) | \mathbf{F}_{\rm inc}(t)\rangle_{V_{\rm res}} \exp(-i\tilde{\omega}_m t) + \langle \tilde{\mathbf{E}}_m | \varepsilon_b - \varepsilon_\infty | \mathbf{E}_{\rm inc}(t)\rangle_{V_{\rm res}}, \tag{8}$$

with $\mathbf{F}_{\rm inc}(t) = \int_{-\infty}^{t} \mathbf{E}_{\rm inc}(t')\exp(i\tilde{\omega}_m t')dt'$. Note that Eq. (8) assumes that the background permittivity ε_b is frequency-independent.

While it may not be the main point of the present work, we would like to stress by the way that the present formalism may also provide a solid theoretical foundation to the temporal coupled-mode theory (CMT) of resonators [41], a famous formalism used to model resonator dynamics. Despite its importance and universality, to our knowledge the temporal CMT still relies nowadays on phenomenological coupling coefficients that are fitted and is restricted to nearly Hermitian resonators with weak loss and couplings [41–43]. In contrast, the following equation in a CMT form that is easy derived from Eq. (8) by applying the derivative with respect to t on both sides of the equation,

$$d\beta_m(t)/dt = -i\tilde{\omega}_m\beta_m(t) + \langle \tilde{\mathbf{E}}_m^* | i\tilde{\omega}_m(\varepsilon(\tilde{\omega}_m) - \varepsilon_\infty) | \mathbf{E}_{\rm inc}(t)\rangle_{V_{\rm res}} + \langle \tilde{\mathbf{E}}_m^* | \varepsilon_b - \epsilon_\infty | d\mathbf{E}_{\rm inc}(t)/dt\rangle_{V_{\rm res}}, \tag{9}$$

provides an analytical and rigorous expression of the coupling coefficient.

The upper panel in Fig. 2(b) shows the temporal evolution of the x component of the electric field at the gap center of the bowtie for a 10-fs plane-wave Gaussian pulse illumination with a central frequency of $0.5\omega_p$ and a bandwidth of $0.058\omega_p$. As evidenced by the comparison with the red curve, they are very accurate, much more than in earlier QNM-expansion works restricted to quasistatic approximations [44] or small truncations numbers [38].

Comparing the computational performance of different methods is difficult. However, we can say that the QNM-expansion method is highly effective. The CPU times to compute the spectral or temporal responses in Fig. 2 with an ordinary desktop computer are only 10 min, which are mainly devoted to the QNM computation, the computation of the modal coefficients being very fast comparatively. The present approach thus shows a convincing potential for fast computations in the temporal domain, and represents an interesting alternative to conventional finite-difference time-domain (FDTD) methods. Additionally, note that any new instance of the driving-field parameters, by varying the pulse duration, polarization, or incidence angle, requires an entirely new computation with the FDTD methods, whereas owing to analyticity, the additional computation with the present approach just requires performing a 1D fast Fourier transform (FFT). Additional details on computational speed as the truncation rank M is varied are provided in Supplemental Material, Sec. 5.2.

The temporal QNM-expansion also provides key clues toward understanding nanoresonator dynamics, since the overall response simply results from the superposition of every individual mode response; see Eq. (7). The bottom panel of

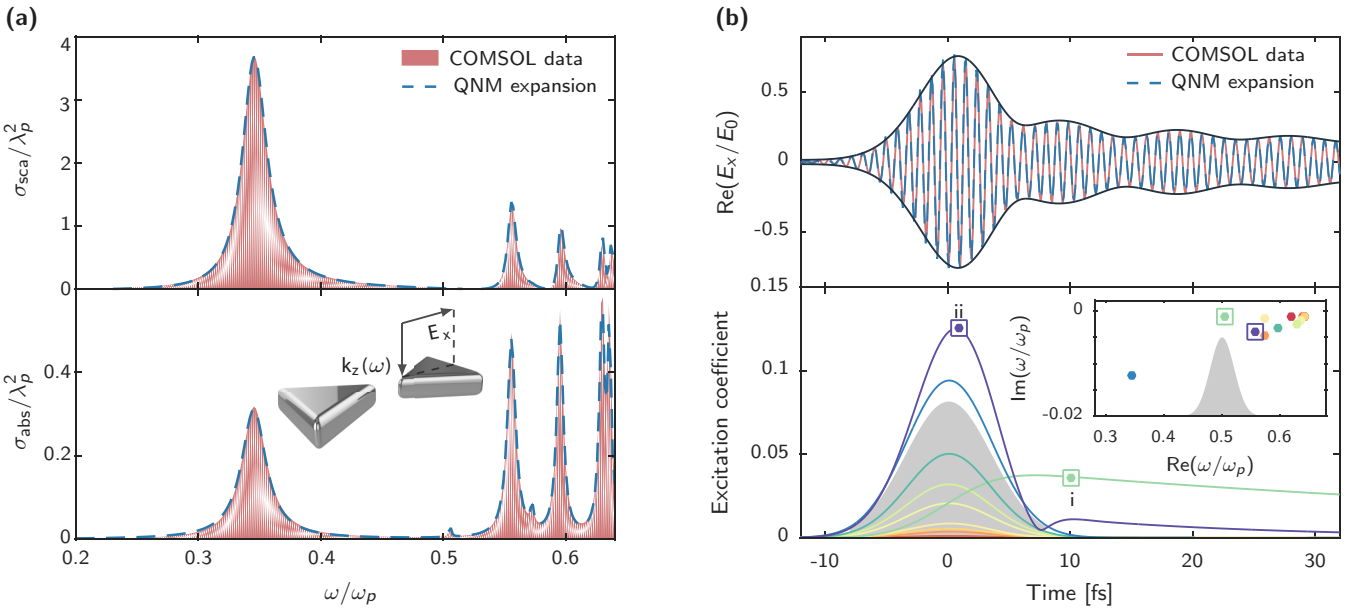

FIG. 2. Validation of the QNM-expansion formalism in the frequency- (a) and time (b) domains. The results hold for the bowtie illuminated by a plane wave polarized along the x direction with expansions composed of 12 QNMs whose energies and decay rates are shown in the inset in (b). (a) Absorption and scattering cross-section spectra. The maximum absolute error between the QNM-expansion results and "COMSOL data" obtained with frequency-domain simulations is smaller than 0.06. (b) Temporal response for a 10-fs plane-wave Fourier-limited Gaussian pulse, whose temporal and spectral envelopes are shown in the lower panel, with the shadowed gray areas. Top: Temporal evolution of E_x (normalized by the maximum amplitude E_0 of the electric field of the incident pulse) at the gap center. The reference COMSOL data are obtained by a Fourier transform of the frequency-domain data. Bottom: Temporal evolution of the QNM excitation coefficients. The two dominant QNMs responsible for the long-tail oscillatory response are highlighted with squares and labeled with "i" and "ii." The inset shows the eigenfrequencies of the 12 QNMs used in the QNM expansion.

Fig. 2(b) shows the time evolution of the excitation coefficients $\beta_m(t)$ of every individual mode obtained by the FFT. To ease the visual analysis, we additionally show the shape of the incident pulse with the shadowed gray curve.

Moreover, from Eq. (8), it is easy to derive an analytic expression of $\beta_m(t)$ for Gaussian pulses; see Eq. (SI.3-38) in Supplemental Material. Equation (SI.3-38) contains the error function and is not fully transparent for interpretation. Better insight can be achieved by mimicking the Gaussian pulse with a simpler mathematical form $\mathbf{E}_{\mathrm{inc}}(\mathrm{t}) = \mathbf{E}_0 \exp(-\mathrm{i}\omega_0 \mathrm{t} - |\mathrm{t}|/\Delta \mathrm{t})$, with $\mathbf{E}_0 = e_0 \exp(i\omega_0 z/c)\hat{\mathbf{x}}$ (e_0 being a constant) and ω_0 the pulse central frequency. Then, $\beta_m(t)$ becomes

$$\begin{aligned} t < 0,\ \beta_m(t) &= C_m^- \exp\left(-i\omega_0 t - |\mathrm{t}|/\Delta t\right), \\ t > 0,\ \beta_m(t) &= C_m^+ \exp\left(-i\omega_0 t - |\mathrm{t}|/\Delta t\right) + \left(C_m^+ - C_m^-\right) \exp\left(-i\tilde{\omega}_m t\right), \end{aligned} \tag{10}$$

with $C_m^{\pm} = \langle \tilde{\mathbf{E}}_m^* | \frac{\tilde{\omega}_m(\varepsilon_m(\tilde{\omega}_m)-\varepsilon_b)}{\tilde{\omega}_m-\omega_0 \pm i/\Delta t} | \mathbf{E}_0 \rangle_{V_{\mathrm{res}}}$, $t = 0$ being the arrival time of the pulse peak at the nanoresonator center $z = 0$. For $t > 0$, it is noticeable that the excitation coefficient has two interference terms with time dependence $\omega_0 t$ and $\tilde{\omega}_m t$. They may result in marked interference features, especially if the two terms have comparable amplitudes for $\omega_{\mathrm{beat}} t \sim 1$, where ω_{beat} is the beating frequency $\mathrm{Re}(\tilde{\omega}_m) - \omega_0$. Additionally, for $|\tilde{\omega}_m - \omega_0| \gg 1/\Delta t$, i.e., for QNM frequencies lying far outside the spectral range of the incident pulse, $|C_m^+ - C_m^-| \ll |C_m^+|, |C_m^-|$, so that $\beta_m(t)$ presents a temporal shape almost identical to that of the incident pulse. These findings well explain the main features of $\beta_m(t)$ observed in Fig. 2(b), as detailed below.

Clearly, the initial bowtie response during the pulse duration Δt is due to all the off-resonant QNMs (unlabeled curves) that all exhibit a response that is very similar to the shape of the incident pulse, in agreement with the analysis in the above paragraph. More interesting is the oscillatory long-tail response at long times, which is understood as a beating between the contributions of the two QNMs labeled "i" and "ii." The green curve with a long tail results from the energy release of a relatively high-Q ($Q \approx 220$) dark mode with an energy matched with the frequency of the driving pulse. The purple curve of the mode labeled "ii" has a surprising shape, with a kink around 8 fs. Following Eq. (10), the kink can be interpreted as resulting from a destructive interference. This interpretation has been further confirmed by directly examining the companion excitation coefficient $\alpha_{ii}(\omega)$, which exhibits two peaks at the central frequency $0.5\omega_p$ of the incident pulse and the QNM energy $\mathrm{Re}(\tilde{\omega}_{ii}) = 0.55\omega_p$, as expected from Eq. (10).

The present physical analysis that emphasizes the contribution of every mode in the dynamics contrasts markedly with the

black sensation left by brute-force numerical methods, which are capable of predicting all the fine details of the dynamics but cannot explain their origin. In the spectral domain, the phenomenon related to mode beating in the temporal domain is mode interference that results in a myriad of steep and asymmetric Fano resonance shapes [45]. In our opinion, the QNM expansion of Eq. (5) is the method of choice to analyze and engineer Fano resonances, as it provides a transparent mathematical support that disentangles the essential roles played by the geometry and the driving-field parameters in altering the Fano line shape.

B. Quenching in nanoresonators

QNM-expansion formalisms are well known for well predicting the spontaneous emission rate enhancements (Purcell effect) of quantum emitters coupled with the dominant resonance modes of plasmonic antennas [12,46,47]. When the emitters approach the metal surfaces down to separation distances smaller than 10 nm, considerable Ohmic heating or quenching is induced at the metal surface just beneath the emitters [48]. Albeit inevitable in plasmonic nanoantennas, quenching has not been previously addressed in the literature on QNM expansions [15], and it appears important to see whether it could be modeled. Incidentally, this will bring us to the important question of the nature of the QNMs responsible for quenching, whose answer will cast doubt on the potential of high-k surface plasmon polariton (SPPs). A second motivation for this study is that quenching always occurs at a precise position in a tiny localized volume that strongly depends on the source position, and since QNMs are intrinsic field maps that reflects the symmetry of the geometry and are independent of the source, the modeling of quenching with QNM expansions represents a serious test, which brings us to the question of the limits of the approach.

For clarification, we consider the emission of an on-axis linearly polarized dipole located at a separation distance d above a silver nanorod in air ($\varepsilon_b = 1$) at a frequency $0.29\omega_p$ matched with the energy of the fundamental dipole resonance of the nanorod. This classical problem has recently received much attention to clarify the connection between the density of electromagnetic states and QNMs [12,14,15]. The numerical predictions obtained with $M = 500$ QNMs are displayed with the dashed blue curve in Fig. 3(a). As d is lowered from 20 to 2 nm, the decay rate rapidly increases from 25 to 200, in excellent agreement with fully vectorial Green-tensor numerical data (red circles) obtained with COMSOL MULTIPHYSICS. To illustrate the step forward realized with the present formalism, we also plot the state-of-the-art results (solid blue curve) obtained in earlier works on QNMs [12,46,47], which were all unable to predict the decay-rate increase for small d's. Consistently, Fig. 3(b) shows the building up of the Ohmic loss just beneath the emitter as the truncation rank M increases.

For a single emitter frequency and position, there is no selective advantage to be gained by computing the Green function with modal expansions at a single frequency, considering that $M = 500$ QNMs are needed for recovering accurate results. However, the computation brings important highlights. First the excellent agreement suggests that, at least in the classical dipole-dipole interaction approximations, quenching is indeed

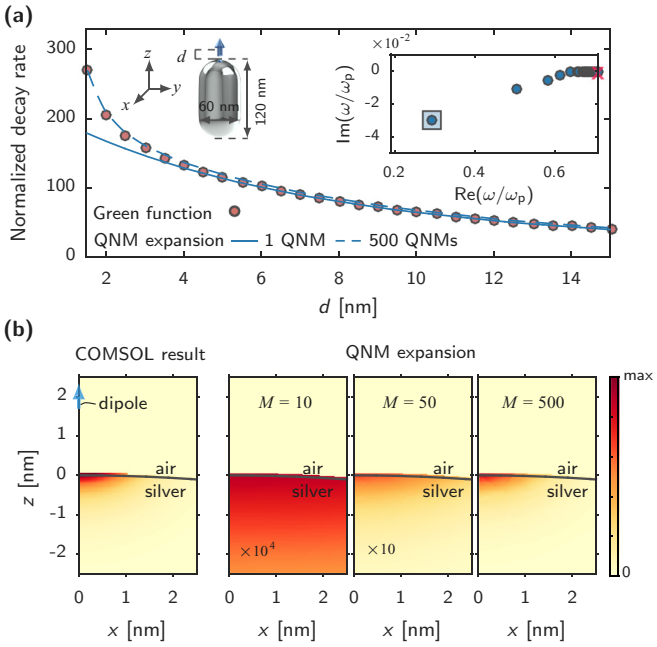

FIG. 3. Modal analysis of quenching in metallic nanoantennas. (a) Normalized decay rate of an on-axis-polarized electric dipole placed at a distance d above a silver nanorod. The dipole emits at the frequency $0.29\omega_p$ matched with the energy of the dominant electric-dipole QNM highlighted by a square in the right inset. The dashed curve computed with $M = 500$ QNMs quantitatively matches the Green-function computational data (red circles) obtained with COMSOL. The solid curve represents the normalized decay rate predicted for $M = 1$ with the dominant electric-dipole QNM, as with all earlier works [12,46,47]. (b) Distribution of the absorbed power density $\omega\mathrm{Im}(\varepsilon)|\mathbf{E}|^2/2$ computed for a dipole (blue arrow) located at 2 nm above the surface and for several truncation orders M. Again, a quantitative agreement is achieved between the distributions computed with the QNM expansion for $M = 500$ (rightmost panel) and COMSOL (leftmost panel), evidencing that the local density of states enhancement due to quenching involves localized-plasmon QNMs, which accumulate at frequencies close to the resonance frequency (highlighted by the red cross in the right inset) of nonretarded slow surface plasmons on flat interfaces.

a direct consequence of the excitation of high-order plasmon modes. Although widely accepted [49], the role played by high-order plasmons received little evidence for simple 1D geometries [50], or not at all for nanoantennas to our knowledge. Second, it is important to evidence the plasmons involved in the quenching. Their complex frequencies are shown in the right inset of Fig. 3(a). Noticeably, quenching arises from a mode accumulation at the surface plasma frequency $\tilde{\omega}_{\mathrm{SP}}$ of high-k SPPs on flat surfaces, defined by $\varepsilon_b = -\varepsilon(\tilde{\omega}_{\mathrm{SP}})$ and identified with a red cross. Intuitively, as d vanishes, the dipole sees a flat interface, and the higher-order plasmons cease to depend on the antenna shape, and resemble those of flat interfaces. Finally, the nature of the modes questions the great virtue attributed to delocalized SPPs on flat surfaces associated with the flat asymptote in the (complex)ω versus (real)k in all applications related to plasmonic super-resolution and confinement [50], since their excitation will be inevitably accompanied with quenching.

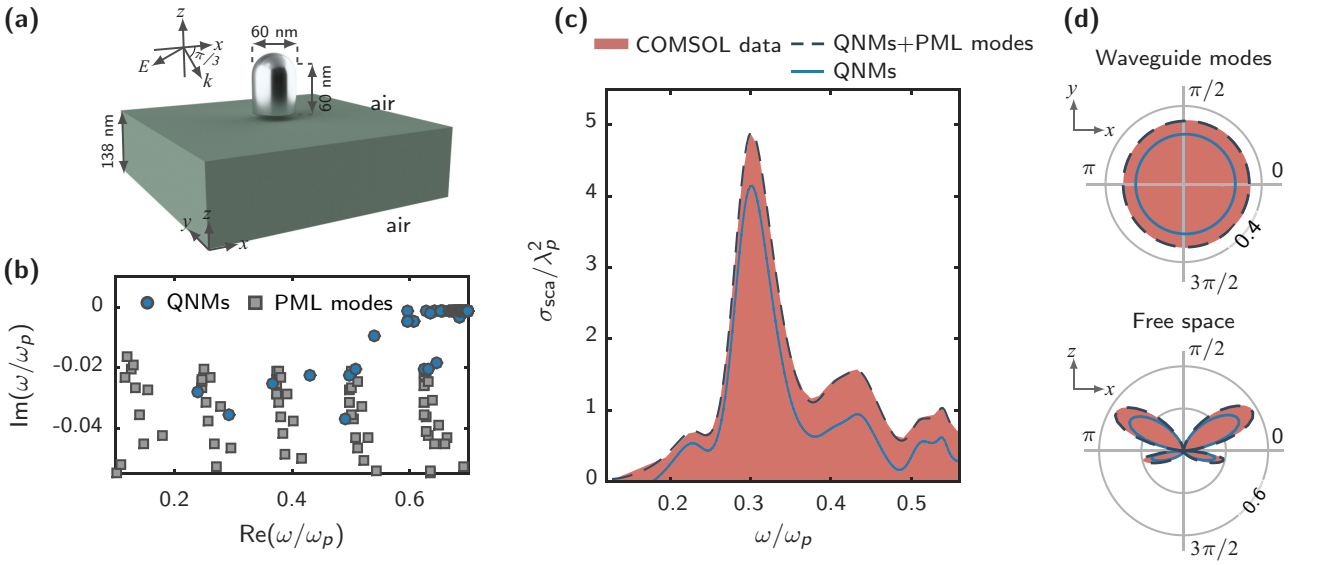

FIG. 4. Importance of PML modes. (a) Schematic representation of a nanobullet on a semiconductor slab with an infinite spatial extension in the transverse x- and y directions. (b) Distribution of the QNM and PML modes eigenfrequencies in the complex plane. (c) Scattering cross-section σ_{sca} under illumination by a TM-polarized plane wave incident at oblique angle ($\theta = 60^\circ$ from the x axis). (d) Angular distributions ($d\sigma_{\text{sca}}/d\Omega\lambda_p^2$ in polar diagrams) of the light intensity radiated into the slab guided modes in the transverse (x,y) plane (top) and into free space in the (x,z) plane (bottom) for $\omega = 0.3\omega_p$. We used the near-to-far-field transforms in Ref. [51] to compute the radiation diagrams. In (c) and (d) the solid-blue and dashed-black curves are computed by retaining 20 QNMs only and 20 QNMs plus 200 PML modes, respectively, and the shadowed pink curves are the data obtained with the frequency-domain solver of COMSOL MULTIPHYSICS. For the reconstruction, the background medium is chosen to be the slab in air, thereby the overlap integrals in Eq. (6) is performed in the nanobullet volume only.

C. Nanoresonators in complex backgrounds: Importance of PML modes

So far, we have considered geometries for which accurate predictions can be achieved with expansions mainly involving QNMs. This is especially possible when the QNM basis is complete, requiring that the Green tensor is analytic in the complex frequency plane excluding the QNM poles [10,11]. QNM-expansion completeness is guaranteed for 3D nanoresonators in a homogeneous background, like in Figs. 1 –3, but breaks down for 2D geometries [15,29] or for 3D geometries for which the background is nonuniform, e.g., nanoresonators laying on thin-film substrates. Mathematically, the breakdown occurs when the Green tensor has branch cuts in the complex frequency plane. Since QNMs and PML-modes together constitute a complete basis for the discretized Maxwell operator in the whole simulation domain (see Sec. II A), when open spaces are mapped onto finite spaces truncated by PMLs, the formal branch cuts of the initial open problem disappear and are replaced by PML modes, which are expected to carry the extra degrees of freedom.

With the last example, our motivation is to study a complex geometry for which it is necessary to include the PML modes in the expansion to achieve an accurate reconstruction. The importance of PML modes for reconstruction has been evidenced so far only for a 2D nondispersive geometry in air [29], to our knowledge. The geometry consists of a silver nanobullet (a nanorod capped with a hemisphere on one side) laying on a 138-nm-thick semiconductor slab with an infinite spatial extent. We have also tested the case of the same nanobullet on a metal substrate and found that the impact of PML modes is a little less stringent; see Supplemental Material, Sec. 5.4.

Figure 4(b) shows the visible spectrum computed with our QNM solver in the spectral interval $[0.1\ \omega_p, 0.7\ \omega_p]$. In comparison with Fig. 1(a), in which PML modes are simply distributed along a tilted straight line, the spectrum appears more complex. The first salient feature is that it includes several vertical branches that are regularly spaced along the horizontal axis. To intuitively understand their origins, we recall from the discussions in Sec. II A that one class of PML modes originates from the continuum of background modes that, for Fig. 4, include slab waveguide modes. We believe that the multiple branches are remnant of the PML-transformed waveguide modes of the semiconductor slab that is truncated by PMLs for numerical purpose. Note that similar branch patterns in the complex plane were also observed for 1D gratings due to the existence of different diffraction orders; see Fig. 11 in Ref. [29].

The second salient feature of the spectrum is the entanglement between PML modes and QNMs, which set close to one another in the complex plane. To discriminate these modes, we exploit the crucial difference between QNMs and PML modes: QNMs are insensitive to PML-parameter variations, whereas PML modes are sensitive. Specifically, QNMs and PML modes are identified by contrasting modes computed with different PMLs. Details are provided in Supplemental Material, Sec. 3.4.

Figure 4(c) shows the scattering cross-section σ_{sca} computed by neglecting or including PML modes in the reconstruction. As expected, we observe that by retaining only QNMs in the expansion, it is not possible to accurately predict σ_{sca}; see the large difference between the blue curve and numerical data obtained with the frequency solver of COMSOL MULTIPHYSICS.

Quite the contrary, it is necessary to retain as many as 200 PML modes in the expansion to achieve a quantitative prediction of the scattering cross section. The same predictive force is obtained in Fig. 4(d) for the far-field radiation diagram into the free-space modes above and underneath the slab and into the guided modes that are launched into the slab. Details on how the accuracy increases by progressively adding PML modes in the expansion are provided in Supplemental Material, Sec. 5.3; see Fig. SI.7. In this supplemental section, we additionally study the convergence rate of a similar geometry in which the same nanobullet is placed above a metal substrate (in replacement of the semiconductor slab); see Fig. SI.8. The intercomparison of the two geometries evidence that the slab case has a slower convergence performance as a function of the number of retained eigenmodes in the expansion. We thus consider that the present example, obtained for a 3D dispersive resonator in a nonuniform background and for a complex spectrum that entangle PML modes and QNMS, constitutes a strong evidence of the generality and soundness of the present method.

V. CONCLUSION

By providing faithful predictions of the dynamics of plasmonic nanoresonators for the general case of complex geometries placed in nonuniform backgrounds, the present QNM-expansion formalism takes an important step toward the deployment of modal theories for analyzing nanoresonators. It features two main building blocks: a FEM-based QNM solver that is robustly applicable for dissipative, dispersive nanoresonators, and a general expression of the modal excitation coefficient for reconstructing scattering fields. The formalism combines the well-known advantages of modal approaches, namely a clarification of the physics as the numerical and physical basis are the same, and an excellent computational performance especially when moderate accuracy is required, when the resonator response is driven by a few dominant modes [15], or when the nanoresonator responses need to be explored for various instances of the driving fields.

Further developments may include refinements of the numerical method, for instance by incorporating dispersive PMLs [1] that allow the computation of QNMs over an extended spectral range. They may also include extensions toward important new applications of nanoresonators at the interface between photonics and other areas of physics, e.g., optomechanical cooling and charge-carrier coupling [52], for which the QNM-expansion formalism is expected to be a smart approach to represent photonic freedoms with dynamically changing modal coefficients that reveal the complex dynamics of the coupled system.

ACKNOWLEDGMENTS

W.Y. acknowledges a fellowship of the Centre National de la Recherche Scientifique (CNRS). The work was supported by the French National Agency for Research (ANR) under the project "Resonance" (Grant No. ANR-16-CE24-0013). This study has been carried out with financial support from the French State, managed by the French National Agency for Research (ANR) in the frame of the "Investments for the Future" Programme IdEx Bordeaux – LAPHIA (Grant No. ANR-10-IDEX-03-02). P.L. is pleased to acknowledge the support from the LabEx LAPHIA and from CNRS. We also thank Shanhui Fan for drawing our attention to the potential of the auxiliary-field method. We thank Mondher Besbes, Kevin Vynck, Christophe Sauvan, Boris Gralak, André Nicolet, and Marc Duruflé for interesting discussions and computational assistance.

[1] A. Taflove, S. G. Johnson, and A. Oskooi, *Advances in FDTD Computational Electrodynamics: Photonics and Nanotechnology* (Artech House, Boston, 2013).

[2] J. M. Jin, *The Finite Element Method in Electromagnetics* (Wiley-IEEE Press, Hoboken, NJ, 2014).

[3] A. W. Snyder and J. Love, *Optical Waveguide Theory* (Springer, US, 1983).

[4] D. Marcuse, *Theory of Dielectric Optical Waveguides* (Academic Press, New York, 1974).

[5] A. J. F. Siegert, On the derivation of the dispersion formula for nuclear reactions, Phys. Rev. **56**, 750 (1939).

[6] C. V. Vishveshwara, Scattering of gravitational radiation by a Schwarzschild black-hole, Nature (London) **227**, 936 (1970).

[7] R. M. More and E. Gerjuoy, Properties of resonance wave functions, Phys. Rev. A **7**, 1288 (1973).

[8] B. J. Hoenders, On the completeness of the natural modes for quantum mechanical potential scattering, J. Math. Phys. **20**, 329 (1979).

[9] C. E. Baum, Interaction Note 88, December 1971. On the singularity expansion method for the solution of electromagnetic interaction problem. See http://www.dtic.mil/cgi-bin/GetTRDoc?Location=U2&doc=GetTRDoc.pdf&AD=ADA066905.

[10] P. T. Leung, S. Y. Liu, and K. Young, Completeness and orthogonality of quasinormal modes in leaky optical cavities, Phys. Rev. A **49**, 3057 (1994).

[11] K. M. Lee, P. T. Leung, and K. M. Pang, Dyadic formulation of morphology-dependent resonances. I. Completeness relation, J. Opt. Soc. Am. B **16**, 1409 (1999).

[12] C. Sauvan, J.-P. Hugonin, I. S. Maksymov, and P. Lalanne, Theory of the Spontaneous Optical Emission of Nanosize Photonic and Plasmon Resonators, Phys. Rev. Lett. **110**, 237401 (2013).

[13] C. Sauvan, J.-P. Hugonin, and P. Lalanne, Photonic and plasmonic nanoresonators: A modal approach, Proc. SPIE, Active Photonic Mater. VII **9546**, 95461C (2015).

[14] E. A. Muljarov and W. Langbein, Exact mode volume and Purcell factor of open optical systems, Phys. Rev. B **94**, 235438 (2016).

[15] P. Lalanne, W. Yan, V. Kevin, C. Sauvan, and J.-P. Hugonin, Light interaction with photonic and plasmonic resonances, Laser Photonics Rev. **4**, 1700113 (2018).

[16] E. A. Muljarov, W. Langbein, and R. Zimmermann, Brillouin-Wigner perturbation theory in open electromagnetic systems, Europhys. Lett. **92**, 50010 (2010).

[17] E. A. Muljarov and W. Langbein, Resonant-state expansion of dispersive open optical systems: Creating gold from sand, Phys. Rev. B **93**, 075417 (2016).

[18] J. Yang, H. Giessen, and P. Lalanne, Simple analytical expression for the peak-frequency shifts of plasmonic resonances for sensing, Nano Lett. **15**, 3439 (2015).

[19] T. Weiss, M. Mesch, M. Schäferling, H. Giessen, W. Langbein, and E. A. Mulfarov, From Dark to Bright: First-Order Perturbation Theory with Analytical Mode Normalization for Plasmonic Nanoantenna Arrays Applied to Refractive Index Sensing, Phys. Rev. Lett. **116**, 237401 (2016).

[20] Q. Bai, M. Perrin, C. Sauvan, J. P. Hugonin, and P. Lalanne, Efficient and intuitive method for the analysis of light scattering by a resonant nanostructure, Opt. Express **21**, 27371 (2013).

[21] J. Zimmerling, L. Wei, P. Urbach, and R. Remis, Efficient computation of the spontaneous decay of arbitrarily shaped 3D nanosized resonators: A Krylov model-order reduction approach, Appl. Phys. A **122**, 158 (2016).

[22] L. Zschiedrich, F. Binkowski, N. Nikolay, O. Benson, G. Kewes, and S. Burger, Riesz projection based theory of light-matter interaction in dispersive nanoresonators, arXiv:1802.01871.

[23] D. A. Powell, Resonant dynamics of arbitrarily shaped meta-atoms, Phys. Rev. B **90**, 075108 (2014).

[24] D. A. Powell, Interference between the modes of an all-dielectric meta-atom, Phys. Rev. Appl. **7**, 034006 (2017).

[25] X. Z. Zheng, V. Volskiy, V. K. Valev, G. A. E. Vandenbosch, and V. V. Moshchalkov, Line position and quality factor of plasmonic resonances beyond the quasi-static limit: A full-wave eigenmode analysis route, IEEE J. Sel. Topics Quantum Electron. **19**, 4600908 (2013).

[26] R. M. Joseph, S. C. Hagness, and A. Taflove, Direct time integration of Maxwell's equations in linear dispersive media with absorption for scattering and propagation of femtosecond electromagnetic pulses, Opt. Lett. **16**, 1412 (1991).

[27] A. Raman and S. Fan, Photonic Band Structure of Dispersive Metamaterials Formulated as a Hermitian Eigenvalue Problem, Phys. Rev. Lett. **104**, 087401 (2010).

[28] N. W. Ashcroft and D. N. Mermin, *Solid State Physics* (Brooks Cole, Belmont, CA, 1976).

[29] B. Vial, A. Nicolet, F. Zolla, and M. Commandré, Quasimodal expansion of electromagnetic fields in open two-dimensional structures, Phys. Rev. A **89**, 023829 (2014).

[30] F. Olyslager, Discretization of continuous spectra based on perfectly matched layers, SIAM J. Appl. Math. **64**, 1408 (2004).

[31] See Supplemental Material at http://link.aps.org/supplemental/10.1103/PhysRevB.97.205422 for detailed derivations and further discussions on numerical performance of the modal method, including the accuracy of the QNM solver and the convergence of the reconstruction as a function of the number of modes retained in the modal expansion. References [1,10,11,12,14,20,21,27,29,33,36,47,51,53–56] are cited in Supplemental Material.

[32] https://www.comsol.com/.

[33] F. Tisseur and K. Meerbergen, The quadratic eigenproblem, SIAM Rev. **43**, 235 (2001).

[34] A toolbox package, including a QNM solver in the form of a COMSOL model sheet and a series of MATLAB codes for computing electromagnetic observables with QNMs and PML modes, is available at the webpage of the authors' group, http://www.lp2n.institutoptique.fr/Membres-Services/Responsables-d-equipe/LALANNE-Philippe.

[35] P. B. Johnson and R. W. Christy, Optical constants of the noble metals, Phys. Rev. B **6**, 4370 (1972).

[36] P. T. Leung, S. Y. Liu, and K. Young, Completeness and time-independent perturbation of the quasinormal modes of an absorptive and leaky cavity, Phys. Rev. A **49**, 3982 (1994).

[37] N. Moiseyev, *Non-Hermitian Quantum Mechanics* (Cambridge University Press, Cambridge, England, 2011).

[38] R. Faggiani, A. Losquin, J. Yang, E. Mårsell, A. Mikkelsen, and P. Lalanne, Modal analysis of the ultrafast dynamics of optical nanoresonators, ACS Photonics **4**, 897 (2017).

[39] M. I. Stockman, S. V. Faleev, and D. J. Bergman, Coherent Control of Femtosecond Energy Localization in Nanosystems, Phys. Rev. Lett. **88**, 067402 (2002).

[40] L. Piatkowski, N. Accanto, and N. F. van Hulst, Ultrafast meets ultrasmall: Controlling nanoantennas and molecules, ACS Photonics **3**, 1401 (2016).

[41] H. A. Haus and W. Huang, Coupled-mode theory, Proc. IEEE **79**, 1505 (1991).

[42] W. Shu, Z. Wang, and S. Fan, Temporal coupled-mode theory and the presence of non-orthogonal modes in lossless multimode cavities, IEEE J. Quant. Electron. **40**, 1511 (2004).

[43] S. Fan, W. Suh, and J. D. Joannopoulos, Temporal coupled mode theory for Fano resonances in optical resonators, J. Opt. Soc. Am. A **20**, 569 (2003)

[44] I. D. Mayergovz, Z. Zhang, and G. Miano, Analysis of Dynamics of Excitation and Dephasing of Plasmon Resonance Modes in Nanoparticles, Phys. Rev. Lett. **98**, 147401 (2007).

[45] B. Luk'yanchuk, N. I. Zheludev, S. A. Maier, N. J. Halas, P. Nordlander, H. Giessen, and C. T. Chong, The Fano resonance in plasmonic nanostructures, Nat. Mater. **9**, 707 (2010).

[46] P. T. Kristensen, C. van Vlack, and S. Hughes, Generalized effective mode volume for leaky optical cavities, Opt. Lett. **37**, 1649 (2012).

[47] R. Ge and S. Hughes, Design of an efficient single photon source from a metallic nanorod dimer: A quasi-normal mode finite-difference time-domain approach, Opt. Lett. **39**, 4235 (2014).

[48] K. H. Drexhage, Interaction of light with monomolecular dye layers, Prog. Opt. **12**, 163 (1974).

[49] P. Anger, P. Bharadwaj, and L. Novotny, Enhancement and Quenching of Single-Molecule Fluorescence, Phys. Rev. Lett. **96**, 113002 (2006).

[50] A. Archambault, T. V. Teperik, F. Marquier, and J. J. Greffet, Surface plasmon Fourier optics, Phys. Rev. B **79**, 195414 (2009).

[51] J. Yang, J.-P. Hugonin, and P. Lalanne, Near-to-far field transformations for radiative and guided waves, ACS Photon. **3**, 395 (2016).

[52] M. Kauranen and A. V. Zayats, Nonlinear plasmonics, Nat. Photonics **6**, 737 (2012).

[53] J. Jackson, *Classical Electromagnetics* (John Wiley, New York, 1999).

[54] G. Hanson and A. Yakovlev, *Operator Theory for Electromagnetics: An Introduction* (Springer-Verlag, New York, 2002).

[55] L. Novotny and B. Hecht, *Principles of Nano-Optics* (Cambridge University Press, New York, 2006).

[56] C. A. Balanis, *Antenna Theory Analysis and Design*, 3rd ed. (Wiley-Interscience, New York, 2005).